# Propofol disrupts alpha dynamics in functionally distinct thalamocortical networks during loss of consciousness

Veronica S. Weiner[a,b,1], David W. Zhou[a,b,c,d,1,2,3] , Pegah Kahali[b,c,1,4], Emily P. Stephen[b,5] , Robert A. Peterfreund[c,e], Linda S. Aglio[e,f] , Michele D. Szabo[c], Emad N. Eskandar[e,g,6], Andrés F. Salazar-Gomez[c,7], Aaron L. Sampson[c,8], Sydney S. Cash[d,e] , Emery N. Brown[a,b,c,e,h,i], and Patrick L. Purdon[c,e,3]

**During propofol-induced general anesthesia, alpha rhythms measured using electroencephalography undergo a striking shift from posterior to anterior, termed anteriorization, where the ubiquitous waking alpha is lost and a frontal alpha emerges. The functional significance of alpha anteriorization and the precise brain regions contributing to the phenomenon are a mystery. While posterior alpha is thought to be generated by thalamocortical circuits connecting nuclei of the sensory thalamus with their cortical partners, the thalamic origins of the propofol-induced alpha remain poorly understood. Here, we used human intracranial recordings to identify regions in sensory cortices where propofol attenuates a coherent alpha network, distinct from those in the frontal cortex where it amplifies coherent alpha and beta activities. We then performed diffusion tractography between these identified regions and individual thalamic nuclei to show that the opposing dynamics of anteriorization occur within two distinct thalamocortical networks. We found that propofol disrupted a posterior alpha network structurally connected with nuclei in the sensory and sensory associational regions of the thalamus. At the same time, propofol induced a coherent alpha oscillation within prefrontal cortical areas that were connected with thalamic nuclei involved in cognition, such as the mediodorsal nucleus. The cortical and thalamic anatomy involved, as well as their known functional roles, suggests multiple means by which propofol dismantles sensory and cognitive processes to achieve loss of consciousness.**

propofol | alpha | synchrony | thalamocortical | intracranial EEG

Propofol-induced general anesthesia alters arousal, but it is unclear how it disrupts sensory or cognitive processing in humans. Like other gamma-aminobutyric acid (GABA)-ergic anesthetic drugs, propofol causes widespread slow oscillations (0.1 to 1 Hz), while frontal alpha (8 to 12 Hz) rhythms emerge and the ubiquitous posterior alpha rhythm disappears (1–5). Slow oscillations are thought to reflect decreased arousal and disrupt cortical function broadly (6). However, the functional significance of the dual frontal and posterior alpha-band phenomena [termed anteriorization in clinical anesthesiology and neurophysiology (7)] and their circuit architectures within the human brain are not fully understood (8). Unlike the slow oscillation, alpha dynamics may underlie propofol's disruptions of sensory and cognitive functions, reframing alpha's ubiquitous role during wakefulness as a sensory processing rhythm. Because the alpha rhythm is generated by thalamocortical mechanisms, anatomical mapping at the cortical and thalamic levels may shed light on the circuitry involved in anteriorization.

We took advantage of two key features of alpha thalamocortical networks to study their brain-wide functional and structural attributes in humans. First, alpha oscillations are coherent within thalamocortical networks, linking thalamic populations with large areas of cortex (9, 10). Therefore, coherence analysis of intracranial recordings offers a way to map the cortical distribution of these oscillatory networks. Second, the connected thalamic and cortical regions form system-specific clusters within the thalamocortical network (11), which have been imaged in vivo using probabilistic tractography analysis of diffusion-weighted magnetic resonance images (MRI) (12, 13).

We collected recordings from hundreds of intracranial channels in surface and depth electrodes implanted in 11 epilepsy patients undergoing propofol anesthesia for surgical explantation (Fig. 1 A–C). In these multivariate time series, we applied global coherence analysis, a cross-spectral dimensionality reduction technique (3, 14), to analyze how the spatial structure of coherent alpha rhythms changed during propofol-induced loss of consciousness (LOC). We used global coherence analysis as a whole-network estimation tool to capture intracranial channels participating in coherent oscillations.

Several sites in the thalamus have been previously studied during propofol anesthesia, but recent evidence for whether propofol increases or decreases alpha synchrony between the cortex and thalamus remains conflicted (5, 15–17). Varying choices of thalamic

## Significance

Although anesthetic drugs are known to lower arousal, it is unclear how anesthesia impacts perceptual and cognitive processing. Diminished arousal has been associated with prominent brain oscillations such as the slow wave, but functional roles for other anesthesia-induced rhythmic changes have not been proposed. During waking states, brain oscillations are understood to be involved in a variety of sensory and cognitive processes mediated by circuits connecting posterior or prefrontal cortices with the thalamus. This study shows that propofol disrupts alpha oscillations (~10 cycles/s) in posterior circuits that mediate sensory processing and induces an alpha oscillation in prefrontal cognitive circuits that normally operate at higher frequencies.

regions recorded in these studies may explain the inconsistency among their findings regarding propofol's effects on alpha-band thalamocortical synchrony. To address this controversy, we traced fiber connections between each thalamic nucleus and the cortical regions that exhibited changes in alpha-band coherent activity.

## Results

We found that prior to loss of consciousness (LOC), alpha rhythms can be observed in intracranial recordings from visual, motor, and auditory cortices (Fig. 1D), consistent with reports of occipital, parietal, and temporal sensory alpha rhythms. After LOC, two rhythms
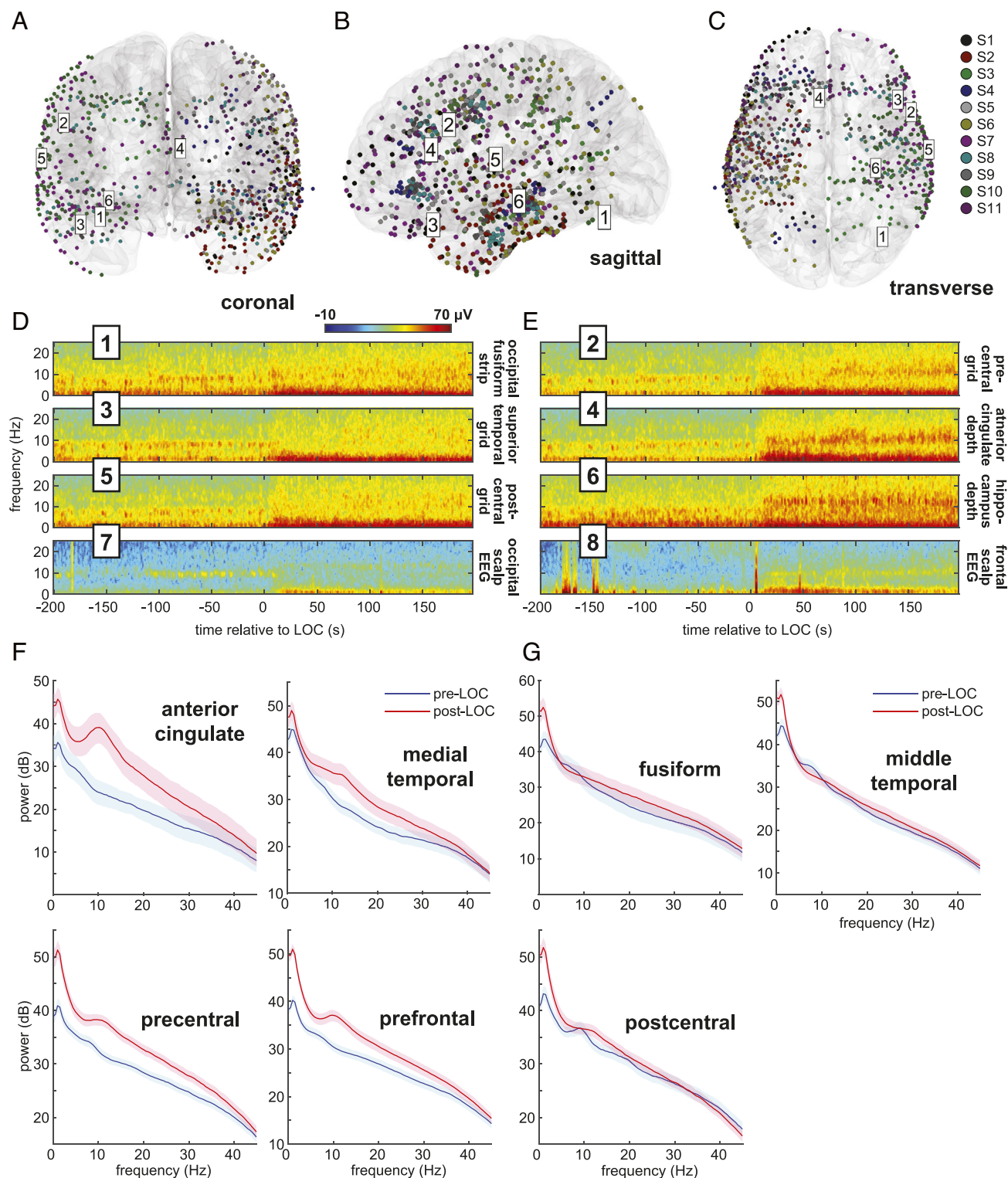


**Fig. 1.** Intracranial electrode coverage and spectral dynamics during propofol-induced general anesthesia. (A–C) Intracranial recordings' (n = 897) spatial coverage. Six intracranial channel locations from one subject are labeled. (D and E) Multitaper spectrograms in selected intracranial and scalp channels of a single subject (S7) aligned to LOC time. After LOC, a waking alpha rhythm in posterior regions (odd-numbered plots) dissipates, while a broader anesthesia-induced alpha rhythm emerges frontally (even-numbered plots). (F and G) Pre- and post-LOC multitaper spectra in selected frontal (F) and posterior (G) regions.

emerge: Alpha rhythms appear in cingulate, frontal, and medial temporal cortices, and slow wave oscillations appear at all locations, as visualized in channel-specific spectrograms. Intracranially recorded alpha rhythms match what occurs in nearby scalp EEG channels recorded concurrently (Fig. 1 *D* and *E*). We identified spatially coherent anterior and posterior alpha rhythms by computing the coherent power spectral density (cPSD) and network-weighted time–frequency signatures from eigendecompositions of the cross-spectral matrix at 10 Hz. (*Materials and Methods*). By comparing cPSD in pre-LOC versus post-LOC epochs across all recording sites, we identified brain regions where propofol increased or decreased the coherent alpha activity (Fig. 2 *A–C*). Propofol achieved its greatest alpha cPSD increases in the cingulate cortices and regions of the frontal lobe, as well as the medial temporal lobe and temporal pole (Fig. 2*F*). Alpha cPSD was attenuated across the inferior, middle, and superior temporal cortices, as well as in the parietal and occipital cortices. Changes in cPSD magnified regional effects typically seen in shifts of 10-Hz spectral power across the combined channel data, improving the spatial resolution of these cortical maps (*SI Appendix*, Fig. S3). These coherent alpha dynamics were sharply linked to loss of consciousness in all recordings, as demonstrated by the network-weighted signatures (Fig. 2 *D* and *E*) of channels coherent at 10 Hz before and after LOC. The post-LOC signature (Fig. 2*E*) also indicates that propofol's frontal signature is more broadband than previously thought, spanning both alpha and beta frequencies.

We used probabilistic tractography to determine whether the alpha networks underlying anteriorization might be structurally connected to distinct nuclei within the human thalamus according to their known functional roles. (*Materials and Methods*). To do so, we matched our data's intracranial electrode coordinates with diffusion-weighted MRI data from the WU-Minn Human Connectome Project (HCP) (18). We found that the posterior alpha network had greater structural connectivity than the anesthesia-induced frontal network to thalamic sensory and sensory association nuclei (Fig. 3). Meanwhile, the anesthesia-induced frontal alpha network had greater structural connectivity than the posterior alpha network to thalamic cognitive-, limbic-, and motor-associated nuclei. Some nuclei, such as the centromedian, central lateral, and medial pulvinar, appeared not to be selectively connected to either network. Our results identify distinct groups of nuclei that may synchronize within each oscillatory network, perhaps through corticothalamic feedback (9). These groups appear to align conspicuously with known system-specific classes of thalamic nuclei: sensory and sensory association on the one hand versus cognitive, limbic, and motor on the other (11).

## Discussion

Overall, our investigation of alpha anteriorization was made possible by collecting a unique dataset from a carefully orchestrated natural experiment of anesthesia using high-density human intracranial recordings, combined with diffusion images from an open repository. Extending previous findings obtained from high-density electroencephalography (4), these results link anterior and posterior coherent alpha networks to known functional divisions of the human cortex situated along the anterior–posterior axis (19, 20),
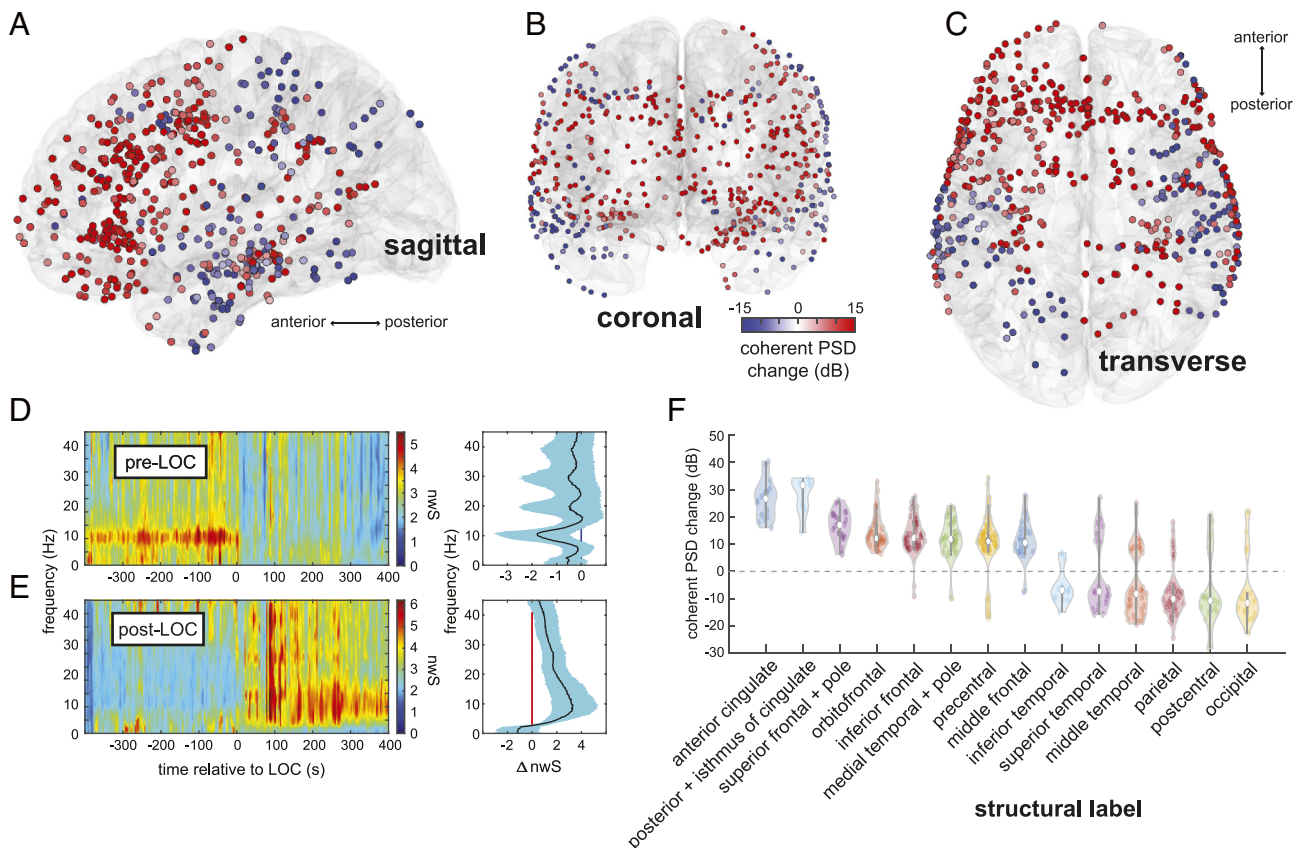


**Fig. 2.** Spatiotemporal mapping of preanesthesia and postanesthesia coherent alpha networks. (*A–C*) Changes in coherent alpha (10-Hz) cPSD across recording sites in all subjects. (*D* and *E*) Pre-LOC global coherence principal components depict a narrow 10-Hz rhythm disappearing at LOC (*D*), and a broader 10-Hz band beginning ~200 s after LOC (*E*). (*F*) cPSD is associated with structural (*F*) parcellations of brain regions. Frontal midline regions such as anterior and posterior cingulate, frontal, and orbitofrontal cortices, as well as the medial temporal lobe, show increased alpha-band cPSD after LOC, whereas posterior regions such as somatosensory and visual areas show a decrease. Constituent labels for each structural category are listed in *SI Appendix*, Table S3.
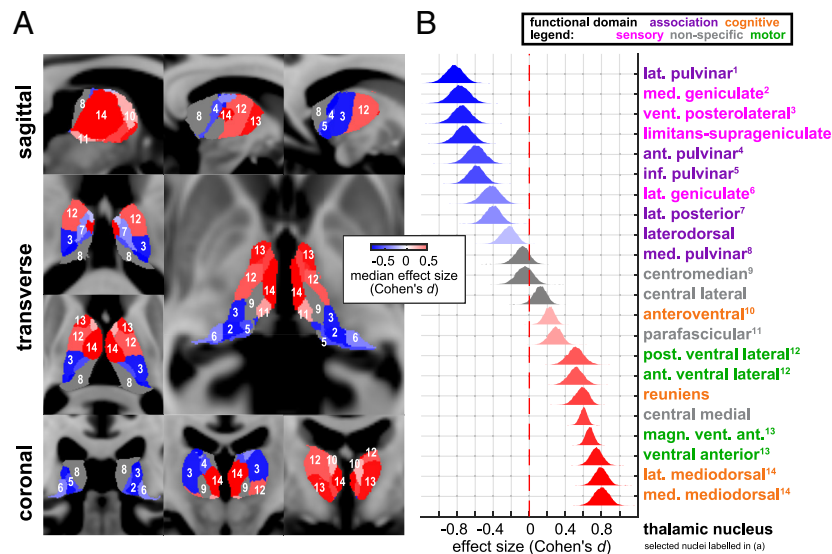
**Fig. 3.** Distinct thalamocortical connections underlying preanesthesia and postanesthesia alpha networks. (*A*) Thalamic nuclei are selectively connected to distinct networks showing either increased or decreased cPSD after LOC. (*B*) Primary and association sensory thalamic nuclei selectively connect to alpha cPSD-decreasing regions; nuclei of the executive and cognitive thalamus selectively connect to alpha cPSD-increasing regions.

which are revealed using diffusion tractography to be connected to distinct thalamic nuclei. Our results also reveal the cortical distribution of propofol's anterior alpha signature in greater detail than previous studies by showing that it engages the cingulate and medial temporal cortices. These medial structures, typically inaccessible to measurement by scalp electroencephalography, have not been previously identified as key structural components of propofol's alpha signature.

Propofol has a number of known biophysical effects that may generate the dual posterior and frontal alpha effects described here. Computational models have suggested multiple mechanisms for thalamic cells (2, 8, 21) to play a role in propofol's diverse alpha-band effects. Propofol increases GABA conductance and decay time, which is thought to slow prefrontal thalamocortical circuits to favor alpha oscillations (2, 22). Propofol also inhibits hyperpolarization-activated membrane currents mediated by hyperpolarization activated cyclic nucleotide gated potassium 1 (HCN1) channels, which is believed to disable thalamocortical circuits responsible for posterior alpha waves (8, 23, 24). These mechanisms may be linked to functionally specialized thalamic nuclei (25, 26). Our results identify circuit-specific locations where propofol may be acting via GABA or HCN1 mechanisms to either generate or disrupt alpha-band activity (8).

It is known that the posterior alpha is driven by first-order sensory thalamic nuclei such as the lateral geniculate (25) and coordinated by higher-order sensory thalamic nuclei such as the pulvinar (27, 28). Similarly, the prefrontal cortex and the mediodorsal nucleus share connections that support thalamocortical and corticocortical synchrony in the alpha and beta frequency ranges (29–31). Previous studies have shown that thalamocortical coherence may either increase or decrease during propofol anesthesia depending on the thalamic nucleus from which recordings were made (5, 15–17). Our work suggests that there is a functional neuroanatomic pattern underlying these disparate accounts in which frontal cortical regions tied to higher-order thalamic nuclei can exhibit higher coherence under propofol, while posterior cortical regions connected to first-order and higher-order sensory thalamic nuclei can exhibit diminished coherence under propofol. Our results provide a whole-thalamus segmentation of nuclei likely participating in the frontal and posterior forms of thalamocortical

coherence. Some of the intralaminar nuclei, including central lateral and centromedian, as well as the medial pulvinar, notably lacked a connectivity preference in this segmentation. The intralaminar nuclei are most commonly associated with ascending arousal and their cortical connections span both anterior and posterior cortical areas. Moreover, the intralaminar nuclei may not directly participate in alpha oscillations. A key result by Redinbaugh et al. has shown that stimulation of the central lateral nucleus increases overall arousal as well as intracolumnar and population alpha coherence in distributed cortical regions (16). Their result is consistent with our findings, in that stimulation of an intralaminar nucleus leading to increased arousal and recovery of consciousness would be predicted to increase alpha coherence in both posterior sensory and sensory associational areas. Other nuclei, such as the medial pulvinar (32), may possess interconnections with key regions such as the frontoparietal network that span both anterior and posterior cortices, also yielding a low connectivity preference in our results.

Recent efforts to define the neural correlates of consciousness propose different roles for the prefrontal and sensory cortices (33–35). Our results suggest that propofol may impair function in both anterior and posterior networks through distinct mechanisms in order to render sensory information in posterior networks inaccessible to prefrontal areas. Functional mechanisms involving alpha and beta oscillations have been found to gate sensory transmission (36), block perceptual integration of sensory information (37–39), and dysregulate attention (28, 40) and working memory (41). In light of these dynamics, we propose two ways by which propofol may disrupt conscious processing via oscillations: 1) By placing posterior thalamocortical networks in a hyperpolarized state (8), which degrades feedforward sensory contents and renders them inaccessible to prefrontal oscillatory feedback, and 2) by inducing a nonphysiological inhibition within the prefrontal–mediodorsal thalamocortical network (2), which restricts its activity to alpha and low-beta bands and interferes with top–down processes. These effects would serve to functionally disrupt feedforward perception on the one hand and feedback control of attention, memory, and executive function on the other. The two anesthesia-induced alpha network changes that we describe would be predicted to impair both bottom–up and top–down processes, respectively. Disruptions of alpha network dynamics

have also been observed in brain states such as traumatic brain injury (42), attention (43), and sleep (44).

In conclusion, our findings provide empirical evidence that anterior and posterior alpha networks modulated by propofol correspond to known functional subdivisions of the cortex and thalamus. In doing so, our results highlight the need for structural specificity in human studies of anesthesia's effects on thalamocortical rhythms. A careful analysis of how propofol compares to other anesthetic drugs with similar or shared mechanisms could further clarify the role that these and other molecular targets play to alter different thalamocortical circuit functions. We note that inhaled ether anesthetics, which also exhibit alpha anteriorization, have GABA and HCN1 mechanisms similar to propofol (45). In contrast, the anesthetic ketamine is known to act via N-methyl-D-aspartate (NMDA) and HCN1 mechanisms. Like propofol, ketamine diminishes posterior alpha activity (46), but it neither produces frontal alpha waves nor engages GABA mechanisms in order to disrupt prefrontal functional networks (47, 48). Future animal studies employing multisite recordings of various thalamocortical circuits, such as those connecting the mediodorsal nucleus with the prefrontal cortex and the pulvinar nucleus with visual cortex, could shed light on the impact of propofol-induced alpha dynamics on specific sensory and cognitive processes. Overall, our study suggests that propofol acts upon two types of thalamocortical circuits through separate alpha mechanisms to impair functions underlying awareness, distinct from the propofol-induced slow oscillation's disruption of arousal.

## Materials and Methods

**Enrollment, Demographics, and Ethics.** We performed intracranial recordings at two hospitals in 14 patients diagnosed with medically intractable epilepsy following long-term epilepsy seizure monitoring prior to electrode explantation and surgical treatment. Three patients were excluded due to high-amplitude broadband noise across the channel array after LOC. Electrode placement was selected by the patients' clinicians without regard to study participation. (Fig. 1 *A–C* and *SI Appendix*, Table S1 for channel type and placement.) Patient demographics and clinical information are listed in *SI Appendix*, Table S1. Study protocols and informed consent procedures were approved by the Institutional Review Boards of Partners HealthCare (Massachusetts General Hospital and Brigham Women's Hospital), and all patients provided fully informed consent. In total, 897 recordings were made from both electrocorticography (ECoG) arrays (containing strip and grid channels) and depth electrodes, and 99 recordings were made from scalp EEG.

**Anesthesia and Behavioral Task.** Prior to surgery, propofol was administered while subjects performed an auditory behavioral task (*SI Appendix*, Fig. S1). All subjects received bolus-dose administration. Bolus doses averaged 154.5 mg, with maximum and minimum dosages at 200 and 70 mg, respectively. Two subjects also received infusions after LOC was achieved. Drug doses and protocols were selected by patients' clinicians without regard to study participation.

Subjects were instructed to perform an auditory button-click task approximately every 4 s over a period spanning administration of anesthesia. Responses were presented and recorded using stimulus presentation software (Presentation, Neurobehavioral Systems, Inc. or EPrime, Psychology Software Tools, Inc.). The time at which loss of consciousness (LOC) occurred was identified by halving the difference between the last correct behavioral response and the first nonresponse following a bolus dose of propofol (*SI Appendix*, Fig. S1). Where accurate responses are unavailable, LOC was assigned to a timepoint 15 s following administration of propofol and prior to start of intubation.

### Data Acquisition and Preprocessing.

*Electrophysiological recordings.* Recordings were made during explantation surgery following 1 to 3 wk of epilepsy monitoring for detection of epileptogenic foci. Signals were acquired prior to anesthetic induction and continued until after anesthetic induction. EEG and intracranial electroencephalography (iEEG) signals were recorded at 2,000, 2,500, or 250 Hz depending on acquisition system

settings. Initial referencing was selected by the patients' clinicians with earlobe (A1/A2), C2, or subdural references when available; otherwise, a common average reference was used. Signals were digitized after applying a high-pass filter above 0.3 Hz (XLTEK, Natus Medical Inc.) (*SI Appendix*, Table S1).

Data were low-pass filtered at 100 Hz using antialiasing finite impulse response (FIR) filters, downsampled to 250 Hz, and then notch filtered at 60 Hz. Data $v(t)$ were then rereferenced using an approximate Laplacian reference for intracranial electrodes in order to isolate local potentials. The rationale against using the common average reference and in favor of using the Laplacian can be found in the study by Cimenser et al. (3). In contrast to bipolar referencing methods, which also isolate field potentials from local regions, the Laplacian reference preserves the exact size of the channel set and has been previously validated for global coherence analysis (3, 4). The Laplacian reference utilized up to $P = 6$ neighbors for each grid electrode and up to $P = 2$ neighbors for strip and depth electrodes using the mean activity in the $P$ channels neighboring a channel $x$ (Eq. 1), and then linearly detrended in each 4-s nonoverlapping time segment $l = 1, \ldots, L$ (Eq. 2), where $a_x^{(l)}$ and $b_x^{(l)}$ are the segment slope and offset values, respectively:

$$j_x(t) = v_x(t) - \frac{1}{P} \sum_{i=1}^{P} v_p^{(i)}(t),$$ [1]

$$z_x^{(l)}(t) = j_x^{(l)}(t) - (a_x^{(l)} t + b_x^{(l)}).$$ [2]

Data segments with missing data or with amplitude greater than 10× the median value across the full recording for each subject were excluded from the global coherence analysis. In individual electrodes, data segments containing epileptiform discharges were excluded from analysis. The total duration of the excluded segments totaled less than 5% of the recorded data. Three patients were excluded from analysis on the basis of generalized epileptiform discharges in the majority of the channels. No data from the remaining subjects were excluded from the network-weighted time–frequency representations.

Two epochs were selected from periods of clean data in each recording and labeled pre-LOC and post-LOC. Pre-LOC epochs were selected from up to a total of 503 s preceding the first propofol dose, and post-LOC epochs were selected from up to a total of 576 s following LOC. The beginning of post-LOC epochs was defined by visual inspection of steady-state spectral power in the median spectrogram occurring after paradoxical excitation, denoted by beta (12 to 25 Hz) and gamma band (30 to 60 Hz) power, and prior to burst suppression, which occurred in five subjects. The post-LOC epoch ended at any of these events: a) the first suppression period apparent in the median spectrogram, b) delivery of any anesthetic drug besides propofol, or c) end of the recording. The consistency of spectral patterns in the selected post-LOC epoch was verified by investigators with expertise in EEG data analysis (V.S.W., D.W.Z., and P.L.P.). (See *SI Appendix*, Fig. S1 for pre-LOC and post-LOC epoch selections.)

*Channel coordinate coregistration and morphing.* Recording electrodes were identified using preoperative T1-weighted MRI and postoperative CT scans in each patient. RAS coordinates were assigned for all intracranial channels by visual inspection of a maximal intensity projection of the CT, and then projected to the subjects' individual MRI spaces using coregistration matrices produced using FreeSurfer. MRI images were processed by FreeSurfer to produce a cortical surface, and channel coordinates were mapped to the nearest surface location using a minimum energy algorithm (49). FreeSurfer was also used to produce structural segmentations and cortical parcellations (50, 51), which were visually verified for each electrode and used to label intracranial depth and surface (grid and strip) electrodes, respectively. Poorly situated channels revealed upon verification were removed from the dataset (n = 25, 2.71% of total implanted channels). Coordinates that were not classified by FreeSurfer were assigned labels manually against the human atlas by Mai et al. (52). Known anatomical regions were assigned to subsets of the structural labels. Individual MRI images were nonlinearly coregistered to an average brain template in FreeSurfer MNI152 space (cvs_avg35_inMNI152) using FreeSurfer's combined volumetric- and surface-based (CVS) algorithm (53, 54). Subject-space channel coordinates were morphed to the average brain space using the CVS coregistration outputs and the FreeSurfer tool applyMorph, employing a procedure similar to the one described in the study by Hamilton et al. (55).

**Patients and channel localization.** We performed intracranial recordings from 897 channels in 11 patients as they underwent anesthetic induction with propofol prior to surgical treatment for medically intractable epilepsy. Patients were asked to perform an auditory behavioral task, and behavioral unresponsiveness was used to define the time of loss of consciousness (LOC). Eight patients ceased task performance within 1 min of bolus induction, one patient ceased performance within 2 min, and two patients were excluded from participation in the task by their clinicians. Channels were implanted throughout all lobes of the cortex, including regions of frontal cortex and the visual, auditory, and somatosensory regions of sensory cortex (Fig. 1 *A–C*), as well as white matter (n = 155) and a small number of subcortical regions (brainstem, amygdala, ventral diencephalon, and ventricle; n = 8). Locations of electrodes were chosen for epilepsy monitoring and without regard to the current study. Cortical regions sampled by electrode recordings in this study include: caudal and rostral anterior cingulate cortices (n = 17), posterior cingulate cortex (n = 5), caudal middle frontal cortex (n = 26), entorhinal cortex (n = 9), frontal pole (n = 3), fusiform gyrus (n = 33), hippocampus (n = 35), inferior frontal gyrus (n = 53), inferior parietal lobe (n = 14), inferior temporal gyrus (n = 49), medial and lateral orbitofrontal cortices (n = 35), middle temporal gyrus (n = 107), postcentral gyrus (n = 45), precentral gyrus (n = 64), rostral middle frontal cortex (n = 65), superior frontal cortex (n = 19), superior temporal gyrus (n = 63), supramarginal gyrus (n = 44), and temporal pole (n = 11).

**Matched diffusion MRI data.** Because high angular resolution diffusion-weighted MRI images were not available for the epilepsy patients enrolled in our study, we assembled a diffusion MRI dataset by matching each nonexcluded epilepsy patient to three healthy human surrogates in the 1200-subject WU-Minn Human Connectome Project (HCP) dataset (18). Surrogates were matched by producing a distance-based ranking of HCP subjects with respect to epilepsy patients using the following demographic and MRI volumetric metrics: age, gender, handedness, brain volume, cortical white matter volume, and thalamic volume (*SI Appendix*, Table S2).

The HCP dataset provided high angular resolution diffusion imaging (dMRI) acquired using the 3 Tesla Siemens Skyra "Connectome" scanner. Full dMRI sessions included six runs with three different gradient tables and oblique axial acquisitions alternating between right-to-left and left-to-right phase encoding directions in consecutive runs. Each gradient table includes approximately 90 diffusion-weighting directions. Diffusion weighting consisted of three shells of b = 1,000, 2,000, and 3,000 s/mm$^2$ interspersed with an approximately equal number of acquisitions on each shell within each run. Six b = 0 acquisitions were interspersed throughout each run.

The dMRI data were preprocessed using the HCP diffusion pipeline (56). The data were further processed with FMRIB Software Library's (FSL's) BEDPOSTX (Bayesian Estimation of Diffusion Parameters Obtained using Sampling Techniques, modeling crossing X fibers) to model white matter fiber orientations and crossing fibers for probabilistic tractography. BEDPOSTX uses Markov Chain Monte Carlo sampling to build probability distributions on diffusion parameters at each voxel (57).

### Data Analysis and Statistics.

**Data segmentation.** In order to capture the structure of coherent dynamics in the brain states of resting state wakefulness and propofol-induced unconsciousness, we segmented periods of stable oscillatory activity in each patient before and after LOC, labeling these epochs pre-LOC and post-LOC, respectively. One of each type of epoch was chosen from each patient's recording, with pre-LOC epochs beginning up to 513 s before LOC and post-LOC epochs terminating up to 775 s after LOC. The median length of pre-LOC epochs was 258 s (IQR = 280 s), and that of post-LOC epochs was 150 s (IQR = 216 s).

**Nonparametric bootstrap analyses.** To account for subject-level spatial, temporal, and group-level uncertainty in the nested electrophysiological and connectivity estimates described in the subsequent data analysis sections, we employed the nonparametric bootstrap and the hierarchical, or multilevel, bootstrap. The multilevel bootstrap technique has been widely applied to account for hierarchically structured data with multiple sources of variation (58, 59). The specific details for each bootstrap technique (levels and iterations) are described in each of the sections in which they appear.

**Multitaper spectral and cross-spectral estimation and the frequency domain bootstrap.** We computed tapered Fourier coefficients at frequency $f$ for each

nonoverlapping time series segment $z_x(t)$ from a channel $x \in N$ in the channel set $N$, as in

$$Z_x^{(k)}(f) = \sum_{t=0}^{T-1} z_x(t)u^{(k)}(t)e^{2\pi f\sqrt{-1}t},$$ [3]

over time $t = 0, \ldots, T-1$ and $k = 1, \ldots, K$, where $u^{(k)}(t)$ is the k-th Slepian taper. In standard multitaper spectrograms, we used K = 3 tapers and 2 s time windows with 0.25 s overlaps. We set f = 10 Hz for alpha frequency analyses.

Then, we computed the $|N| \times |N|$ cross-spectral matrix $\mathbf{C}_{xy}^{(k)}(f)$ wherein an element in row $x$ and column $y$ represents the cross-spectrum between channels $x$ and $y$ for each respective taper and time segment:

$$\mathbf{C}_{xy}^{(k)}(f) = Z_x^{(k)}(f)Z_y^{(k)}(f)^H,$$ [4]

where $Z_y^{(k)}(f)^H$ is the complex conjugate transpose of the vectorized tapered Fourier estimates $Z_y^{(k)}(f)^H$. For global coherence analysis, we used $K = 15$ tapers, with non-overlapping time windows of 4 s and a half-bandwidth of 2 Hz. In network-weighted time-frequency plots (Eq. 10), we computed spectrograms using the same multitaper parameters with step sizes of 0.1 s.

For statistical inferences about the output eigenvalues and eigenvectors, we implemented a nonparametric resampling approach for the multitaper-cross-spectral matrix using a frequency-domain bootstrap (FDB) approach to resampling multitaper cross-spectral matrix for a given epoch. Proceeding under the assumption that the tapered estimates $\widehat{\mathbf{C}}_{xy}^{(k)}$ of $\mathbf{C}_{xy}$ are statistically independent in a given non-overlapping time segment $l = 1, 2, \ldots, L$ of the epoch, we followed the nonparametric approach to resample the average cross-spectrum with replacement (60). To create a bootstrap replicate $\widehat{\mathbf{C}}_{xy}^{(k,l)*}(f)$ given $f$, $x$, and $y$, we independently drew K rows and L columns from each matrix of samples $\{\mathbf{C}_{xy}^{(k,l)}(f): k = 1, \ldots, K; l = 1, \ldots, L\}$. Then, we computed the mean across tapers, and the median across time segments for the real and imaginary components of the multitaper mean separately (61):

$$\widehat{\mathbf{C}}_{xy}^*(f) = \operatorname*{med}_{l \in L}\left[ \operatorname{Re}\left( \frac{1}{K}\sum_{k=1}^{K} \mathbf{C}_{xy}^{(k,l)*}(f) \right) \right]$$
$$+ \operatorname*{med}_{l \in L}\left[ \operatorname{Im}\left( \frac{1}{K}\sum_{k=1}^{K} \mathbf{C}_{xy}^{(k,l)*}(f) \right) \right].$$ [5]

We repeated this procedure to generate $B = 200$ bootstrap replicates of the multitaper cross-spectral matrix per frequency, per epoch (pre-LOC and post-LOC), and per subject. Our resampling procedure can be considered a nonoverlapping block bootstrap in the frequency domain (62). All subsequent global coherence computations were performed upon each replicate matrix.

**Global coherence analysis: Cross-spectral matrix eigen decomposition.** To identify frequency-wise coherent networks across the intracranial recording dataset, we used global coherence analysis, a frequency-domain principal component analysis of the cross-spectral matrix (3, 14). In comparison to standard coherence-based network analyses that compute network edge strengths using pair-wise coherence as a coupling function, global coherence analysis estimates whole networks from the principal components of the cross-spectral matrix at a frequency $f$. (Please see the *Materials and Methods* subsection, *Network-weighted time–frequency analysis*, for the precise definition of the term "network" in this study). We applied eigendecompositions to every bootstrap replicate of the multitaper cross-spectral matrix to obtain empirical distributions of eigenvectors, eigenvalues, coherent power spectral density, and other derivatives of global coherence outputs (63):

$$\widehat{\mathbf{C}}_{xy}^*(f) = \mathbf{U}^*(f)\Lambda^*(f)\mathbf{U}^*(f)^H = \sum_{i=1}^{N} \lambda_i^*(f)\mathbf{u}_i^*(f)\mathbf{u}_i^*(f)^H.$$ [6]

This decomposition represents multichannel spectral power in terms of orthonormal bases of coherent activity among channels, effectively summarizing the coherent activity at each frequency. Altogether, the eigendecompositions performed at 10 Hz captured on average 41.29% ($\pm$ 15.58%) of the variance in the pre-LOC data and 48.60% ($\pm$ 20.64%) in the post-LOC data.

**Cross-spectral matrix reconstruction.** In order to estimate the amount of coherent spectral power contributed by individual channels that is captured by the eigenmodes, we reconstructed the cross-spectral matrices using the top three principal components:

$$\widehat{\mathbf{C}}^{*}_{xy}(f) = \sum_{i=1}^{3} \lambda_i^*(f) \mathbf{u}_i^*(f) \mathbf{u}_i^*(f)^H.$$ [7]

Across all analyses, we chose to include the top three components to balance parsimony and representation accuracy. We refer to the diagonal elements $c_{xx}^*(f)$ of $\widehat{\mathbf{C}}'_{xy}(f)$ as the coherent power spectral density (cPSD).

We estimated the difference in replicated means of the cPSD $\Delta c_{xx}^*(f) = \overline{c}_{xx}^{-post*}(f) - \overline{c}_{xx}^{-pre*}(f)$ using the bootstrap. We assessed the empirical cumulative distribution functions $\widehat{F}_x(h) = \frac{1}{B'} \sum_{i=1}^{B'} \mathbf{1}_{\Delta c_{xx}^{(i)*} \le h}$ with $B' = 10^4$ in order to partition the entire set $N$ of intracranial channels into three subsets: $N_{\alpha\uparrow} = \left\{ x \in N \widehat{F}_x(0) < 0.05 \right\}$, $N_{\alpha\downarrow} = \left\{ x \in N \widehat{F}_x(0) > 0.95 \right\}$ and $N_{\alpha\emptyset} = \left\{ x \in N | 0.05 \le \widehat{F}_x(0) \le 0.95 \right\}$ reflecting channels with increasing or decreasing mean coherent power change beyond a 95% confidence level and channels for which the previous two conditions do not apply.

**Network-weighted time–frequency analysis.** In this study, coherence-based networks are defined as a set of weights across all recording channels representing the degree to which they participate in multivariate synchrony. To estimate networks in a frequency band (such as alpha), we used estimates of $c_{xx}^*(g)$ at $g = 10$ Hz frequency to compute weights $w_x^*(g)$ for a given epoch and subject (Eq. 8). To visualize the time–frequency activity represented by these network weights over frequencies $f$ and time segments $l$, we estimate the network-weighted spectrum $\widehat{nwS}(f, g)$, which summarizes the spectrogram across channels $i \in N$ using $w_x^*(g)$ as weights applied to each channel's spectrogram (Eqs. 9 and 10). The number of channels $|N|$ is added as a scaling term to allow comparison between datasets with different numbers of channels.

$$w_x^*(f) = \frac{c_{xx}^*(f)}{\sum_i^N c_{ii}^*(f)},$$ [8]

$$\widehat{S}_x^{(l)}(f) = \frac{1}{K} \sum_{k=1}^{K} \left| \left| Z_x^{(k,l)}(f) \right| \right|^2,$$ [9]

$$\widehat{nwS}^{(l)}(f, g) = \frac{1}{B} \sum_{b=1}^{B} \frac{|N| \sum_{i=1}^{N} w_i^{(b)*}(g) \widehat{S}_i^{(l)}(f)}{\sum_{i=1}^{N} \widehat{S}_i^{(l)}(f)}.$$ [10]

Observe in Eq. 10 that a network represented by a set of equal weights $w_x = \frac{1}{|N|}$ for all channels $x \in N$ would yield a network-weighted time–frequency representation equal to 1 for all $f$ and $l$; likewise, time–frequency activity overrepresented by only a few heavily weighted channels in $w_x(g)$ would result in values of $\widehat{nwS}^{(l)}(f, g)$ substantially greater than 1. The mean $\widehat{nwS}^{(l)}(f, 10)$ across replicates was computed per subject. In the plots shown in Fig. 2 D and E, a two-dimensional median filter with a sliding window of 4 s and 4 Hz was applied to the group-level median network-weighted spectrum. To estimate the overall net change in frequency-domain activity in a network of interest, we computed the group-level mean network-weighted spectral shift $\widehat{\Delta nwS}^{(l)}(f, 10)$ of an alpha network from pre-LOC and post-LOC, using a two-level hierarchical bootstrap of the mean over 1,000 iterations: the first level over subjects (sampled with replacement) and the second level over time segments in each epoch (sampled with replacement per subject) (64). Group-level temporal epochs were chosen using all time windows before 0 s and after 200 s for pre-LOC and post-LOC, respectively,

given that each LOC in each subject is aligned at 0 s and the majority of time-varying artifacts diminish after 200 s.

**Probabilistic tractography.** We performed a probabilistic tractography analysis (57) using matched diffusion-weighted MRI datasets from the WU-Minn Human Connectome Project (HCP) (18). The intracranial electrophysiology data analysis described above yielded two subsets of channels $N_{\alpha\uparrow}$ and $N_{\alpha\downarrow}$ across subjects in which the alpha-band cPSD significantly increased or decreased from pre-LOC to post-LOC, respectively. We used the channel coordinates to produce seed regions of interests (ROIs) for tractography analysis. To ensure accurate tracing along white matter tracts, we centered the cortical seed masks at the point on the white matter surface closest to the channel coordinates. For broader sampling of the brain region in the vicinity of each channel, we dilated the seed masks to a 2-mm sphere. To generate thalamic targets, we obtained a probabilistic atlas developed by Iglesias and coauthors (65) and created masks based on 22 nuclei on each side. We used separate masks for the right and left sides of each nucleus, resulting in 44 masks in total. Using FSL's PROBTRACKX2 (probabilistic tracking with crossing fibres) (57), we traced streamlines from each channel's seed mask to all thalamic nuclei using FSL Classification Targets, using 5,000 streamlines per voxel in seed masks. We performed tractography analysis for each patient using that patient's matched samples of diffusion-weighted images.

In order to account for intersubject variability in diffusion estimates, each subject from our study was matched with three surrogates in the HCP database according to demographic and brain volumetric indices. Multiple studies have used HCP subjects as surrogates or references for patients in separate datasets, including epilepsy patients (66, 67). ROIs associated with thalamic nucleus membership were defined using a thalamic atlas created by Iglesias and coauthors (65). We used these thalamic ROIs as targets for traces made from seed coordinates belonging to electrodes in either the frontal or posterior alpha networks.

The specificity of the thalamocortical connection to each nucleus was estimated for the seed masks belonging to the channel sets $N_{\alpha\uparrow}$ and $N_{\alpha\downarrow}$. The number of streamlines reaching each thalamic nucleus from seeds of the channel sets $N_{\alpha\uparrow}$ and $N_{\alpha\downarrow}$ was normalized by the total number of streamlines reaching the whole thalamus as well as the size of the given thalamic nucleus (number of voxels). We refer to this quantity as the ROI's thalamic nucleus connectivity:

$$\kappa(r_i \to Tn | r_i \to Th) = \frac{s_{r_i \to Tn}}{\text{size}(Tn) \sum_{j=1}^{44} s_{r_i \to Tn_j}},$$ [11]

where $s_{r_i \to Tn}$ is the number of total streamlines between a seed mask ROI $r$ belonging to channel $i \in N_{\alpha\uparrow}$ or $N_{\alpha\downarrow}$ and the mask of a thalamic nucleus $Tn$, and where $Th$ is the union of all thalamic nucleus masks.

We wondered whether streamlines from a cortical ROI to a contralateral thalamic nucleus would be anatomically plausible. In primary-level sensory thalamocortical pathways, they are considered not to be; however, there is evidence in nonhuman primates that frontal areas may connect bilaterally (32, 68). Therefore, we calculated two versions of $\kappa$: one in which each $Tn$ is the union of left and right nucleus masks and another in which each $Tn$ is defined strictly as the nucleus ipsilateral to the respective cortical ROI $r_i$.

To infer the connection preference of a given thalamic nucleus to regions covered by either $N_{\alpha\uparrow}$ or $N_{\alpha\downarrow}$, we calculated the empirical probability distributions of the effect size (Cohen's d) between thalamus nucleus connectivity values of ROIs in $N_{\alpha\uparrow}$ and $N_{\alpha\downarrow}$:

$$d^*(Tn) = \frac{\overline{\kappa}_i^* - \overline{\kappa}_j^*}{\text{std}_{pooled}(\kappa_i^*, \kappa_j^*)},$$ [12]

where $\kappa_i \in \left\{ \kappa(r_i \to Tn | r_i \to Th) \, \forall i \in N_{\alpha\uparrow} \right\}$ and $\kappa_j \in \left\{ k(r_j \to Tn r_j \to Tn) \, \forall j \in N_{\alpha\downarrow} \right\}$. Over 10,000 iterations, we resampled the effect size with a similar two-level hierarchical technique as described above, using surrogate subjects at the first level and regions in $N_{\alpha\uparrow}$ or $N_{\alpha\downarrow}$ as the second. Fig. 3 uses the bilateral version of $\kappa$. (See *SI Appendix*, Fig. S5 for the ipsilateral version).

To characterize the null condition in which channels included in regions $N_{\alpha\uparrow}$ and $N_{\alpha\downarrow}$ were randomly assigned, we reshuffled the channels in the two groups and repeated the effect size computations above (*SI Appendix*, Fig. S6).

Author affiliations: ªDepartment of Brain and Cognitive Sciences, Massachusetts Institute of Technology, Cambridge, MA 02139; ᵇPicower Institute for Learning and Memory, Massachusetts Institute of Technology, Cambridge, MA 02139; ᶜDepartment of Anesthesia, Critical Care and Pain Medicine, Massachusetts General Hospital, Boston, MA 02114; ᵈCenter for Neurotechnology and Recovery, Department of Neurology, Massachusetts General Hospital, Boston, MA 02114; ᵉHarvard Medical School, Boston, MA 02115; ᶠDepartment of Anesthesiology, Perioperative and Pain Medicine, Brigham and Women's Hospital, Boston, MA 02115; ᵍDepartment of Neurological Surgery, Massachusetts General Hospital, Boston, MA 02114; ʰDivision of Health Sciences and Technology, Harvard Medical School/Massachusetts Institute of Technology, Cambridge, MA 02139; and ⁱInstitute of Medical Engineering and Sciences, Massachusetts Institute of Technology, Cambridge, MA 02139

1. V. A. Feshchenko, R. A. Veselis, R. A. Reinsel, Propofol-induced alpha rhythm. *Neuropsychobiology* **50**, 257–266 (2004).
2. S. Ching, A. Cimenser, P. L. Purdon, E. N. Brown, N. J. Kopell, Thalamocortical model for a propofol-induced α-rhythm associated with loss of consciousness. *Proc. Natl. Acad. Sci. U.S.A.* **107**, 22665–22670 (2010).
3. A. Cimenser et al., Tracking brain states under general anesthesia by using global coherence analysis. *Proc. Natl. Acad. Sci. U.S.A.* **108**, 8832–8837 (2011).
4. P. L. Purdon et al., Electroencephalogram signatures of loss and recovery of consciousness from propofol. *Proc. Natl. Acad. Sci. U.S.A.* **110**, E1142–E1151 (2013).
5. F. J. Flores et al., Thalamocortical synchronization during induction and emergence from propofol-induced unconsciousness. *Proc. Natl. Acad. Sci. U.S.A.* **114**, E6660–E6668 (2017).
6. L. D. Lewis et al., Rapid fragmentation of neuronal networks at the onset of propofol-induced unconsciousness. *Proc. Natl. Acad. Sci. U.S.A.* **109**, E3377–E3386 (2012).
7. J. H. Tinker, F. W. Sharbrough, J. D. Michenfelder, Anterior shift of the dominant EEG rhytham during anesthesia in the Java monkey: Correlation with anesthetic potency. *Anesthesiology* **46**, 252 (1977).
8. S. Vijayan, S. Ching, P. L. Purdon, E. N. Brown, N. J. Kopell, Thalamocortical mechanisms for the anteriorization of α rhythms during propofol-induced unconsciousness. *J. Neurosci.* **33**, 11070–11075 (2013).
9. D. Contreras, A. Destexhe, T. J. Sejnowski, M. Steriade, Control of spatiotemporal coherence of a thalamic oscillation by corticothalamic feedback. *Science* **274**, 771–774 (1996).
10. E. G. Jones, The thalamic matrix and thalamocortical synchrony. *Trends Neurosci.* **24**, 595–601 (2001).
11. J. W. Scannell, G. A. Burns, C. C. Hilgetag, M. A. O'Neil, M. P. Young, The connectional organization of the cortico-thalamic system of the cat. *Cereb Cortex.* **9**, 277–299 (1999).
12. T. E. J. Behrens et al., Non-invasive mapping of connections between human thalamus and cortex using diffusion imaging. *Nat. Neurosci.* **6**, 750–757 (2003).
13. D. Zhang, A. Z. Snyder, J. S. Shimony, M. D. Fox, M. E. Raichle, Noninvasive functional and structural connectivity mapping of the human thalamocortical system. *Cereb Cortex.* **20**, 1187–1194 (2010).
14. P. Mitra, *Observed Brain Dynamics* (Oxford University Press, 2007).
15. M. Malekmohammadi, C. M. Price, A. E. Hudson, J. A. T. DiCesare, N. Pouratian, Propofol-induced loss of consciousness is associated with a decrease in thalamocortical connectivity in humans. *Brain* **142**, 2288–2302 (2019), 10.1093/brain/awz169.
16. M. J. Redinbaugh et al., Thalamus modulates consciousness via layer-specific control of cortex. *Neuron* **106**, 66–75.e12 (2020), 10.1016/j.neuron.2020.01.005.
17. A. M. Bastos et al., Neural effects of propofol-induced unconsciousness and its reversal using thalamic stimulation. *Elife* **10**, e60824 (2021), 10.7554/eLife.60824.
18. D. C. Van Essen et al., The WU-Minn Human Connectome Project: An overview. *Neuroimage* **80**, 62–79 (2013).
19. M. Rosanova et al., Natural frequencies of human corticothalamic circuits. *J. Neurosci.* **29**, 7679–7685 (2009).
20. E. Barzegaran, V. Y. Vildavski, M. G. Knyazeva, Fine structure of posterior alpha rhythm in human EEG: Frequency components, their cortical sources, and temporal behavior. *Sci. Rep.* **7**, 8249 (2017).
21. S. Vijayan, N. J. Kopell, Thalamic model of awake alpha oscillations and implications for stimulus processing. *Proc. Natl. Acad. Sci. U.S.A.* **109**, 18553–18558 (2012).
22. D. Bai, P. S. Pennefather, J. F. MacDonald, B. A. Orser, The general anesthetic propofol slows deactivation and desensitization of GABA(A) receptors. *J. Neurosci.* **19**, 10635–10646 (1999).
23. S.-W. Ying, S. Y. Abbas, N. L. Harrison, P. A. Goldstein, Propofol block of Ih contributes to the suppression of neuronal excitability and rhythmic burst firing in thalamocortical neurons: Propofol inhibition of thalamic Ih. *Eur. J. Neurosci.* **23**, 465–480 (2006).
24. A. K. Lyashchenko, K. J. Redd, J. Yang, G. R. Tibbs, Propofol inhibits HCN1 pacemaker channels by selective association with the closed states of the membrane embedded channel core. *J. Physiol.* **583**, 37–56 (2007).
25. S. W. Hughes et al., Synchronized oscillations at α and θ frequencies in the lateral geniculate nucleus. *Neuron* **42**, 253–268 (2004).
26. S. W. Hughes et al., Thalamic gap junctions control local neuronal synchrony and influence macroscopic oscillation amplitude during EEG alpha rhythms. *Front. Psychol.* **2**, 193 (2011).
27. F. H. Lopes da Silva, J. E. Vos, J. Mooibroek, A. Van Rotterdam, Relative contributions of intracortical and thalamo-cortical processes in the generation of alpha rhythms, revealed by partial coherence analysis. *Electroencephalogr. Clin. Neurophysiol.* **50**, 449–456 (1980).
28. Y. B. Saalmann, M. A. Pinsk, L. Wang, S. Kastner, X. Li, The pulvinar regulates information transmission between cortical areas based on attention demands. *Science* **337**, 753–756 (2012).
29. S. Parnaudeau et al., Inhibition of mediodorsal thalamus disrupts thalamofrontal connectivity and cognition. *Neuron* **77**, 1151–1162 (2013).
30. N. A. Ketz, O. Jensen, R. C. O'Reilly, Thalamic pathways underlying prefrontal cortex-medial temporal lobe oscillatory interactions. *Trends Neurosci.* **38**, 3–12 (2015).
31. Y. B. Saalmann, Intralaminar and medial thalamic influence on cortical synchrony, information transmission and cognition. *Front Syst. Neurosci.* **8**, 83 (2014).
32. T. M. Preuss, P. S. Goldman-Rakic, Crossed corticothalamic and thalamocortical connections of macaque prefrontal cortex. *J. Comp. Neurol.* **257**, 269–281 (1987).
33. M. Boly et al., Are the neural correlates of consciousness in the front or in the back of the cerebral cortex? Clinical and neuroimaging evidence. *J. Neurosci.* **37**, 9603–9613 (2017).
34. B. Odegaard, R. T. Knight, H. Lau, Should a few null findings falsify prefrontal theories of conscious perception? *J. Neurosci.* **37**, 9593–9602 (2017).
35. D. Pal et al., Differential role of prefrontal and parietal cortices in controlling level of consciousness. *Curr Biol.* **28**, 2145–2152.e5 (2018).
36. O. Jensen, A. Mazaheri, Shaping functional architecture by oscillatory alpha activity: Gating by inhibition. *Front Hum. Neurosci.* **4**, 186 (2010).
37. N. A. Busch, J. Dubois, R. VanRullen, The phase of ongoing EEG oscillations predicts visual perception. *J. Neurosci.* **29**, 7869–7876 (2009).
38. J. Samaha, B. R. Postle, The speed of alpha-band oscillations predicts the temporal resolution of visual perception. *Curr Biol.* **25**, 2985–2990 (2015).
39. J. Misselhorn, U. Friese, A. K. Engel, Frontal and parietal alpha oscillations reflect attentional modulation of cross-modal matching. *Sci. Rep.* **9**, 5030 (2019).
40. R. Sokoliuk et al., Two spatially distinct posterior alpha sources fulfill different functional roles in attention. *J. Neurosci.* **39**, 7183–7194 (2019).
41. M. Lundqvist et al., Gamma and beta bursts underlie working memory. *Neuron* **90**, 152–164 (2016).
42. S. T. Williams et al., Common resting brain dynamics indicate a possible mechanism underlying zolpidem response in severe brain injury. *Elife* **2**, e01157 (2013).
43. Z. Chen, R. D. Wimmer, M. A. Wilson, M. M. Halassa, Thalamic circuit mechanisms link sensory processing in sleep and attention. *Front. Neural. Circuits* **9**, 83 (2015).
44. M. J. Prerau et al., Tracking the sleep onset process: An empirical model of behavioral and physiological dynamics. *PLoS Comput. Biol.* **10**, e1003866 (2014).
45. H. C. Hemmings Jr., et al., Towards a comprehensive understanding of anesthetic mechanisms of action: A decade of discovery. *Trends Pharmacol. Sci.* **40**, 464–481 (2019).
46. P. E. Vlisides et al., Neurophysiologic correlates of ketamine sedation and anesthesia: A high-density electroencephalography study in healthy volunteers. *Anesthesiology* **127**, 58–69 (2017).
47. B. Moghaddam, B. Adams, A. Verma, D. Daly, Activation of glutamatergic neurotransmission by ketamine: A novel step in the pathway from NMDA receptor blockade to dopaminergic and cognitive disruptions associated with the prefrontal cortex. *J. Neurosci.* **17**, 2921–2927 (1997), 10.1523/jneurosci.17-08-02921.1997.
48. N. Gass et al., Sub-anesthetic ketamine modulates intrinsic BOLD connectivity within the hippocampal-prefrontal circuit in the rat. *Neuropsychopharmacology* **39**, 895–906 (2014).
49. A. R. Dykstra et al., Individualized localization and cortical surface-based registration of intracranial electrodes. *Neuroimage* **59**, 3563–3570 (2012).
50. B. Fischl et al., Whole brain segmentation: Automated labeling of neuroanatomical structures in the human brain. *Neuron* **33**, 341–355 (2002).
51. B. Fischl, Automatically parcellating the human cerebral cortex. *Cereb Cortex* **14**, 11–22 (2004).
52. J. K. Mai, M. Majtanik, G. Paxinos, *Atlas of the Human Brain* (Academic Press, 2015).
53. G. Postelnicu, L. Zollei, B. Fischl, Combined volumetric and surface registration. *IEEE Trans Med. Imaging* **28**, 508–522 (2009).
54. L. Zöllei, A. Stevens, K. Huber, S. Kakunoori, B. Fischl, Improved tractography alignment using combined volumetric and surface registration. *Neuroimage* **51**, 206–213 (2010).

55. L. S. Hamilton, D. L. Chang, M. B. Lee, E. F. Chang, Semi-automated anatomical labeling and inter-subject warping of high-density intracranial recording electrodes in electrocorticography. *Front. Neuroinform.* **11**, 62 (2017).
56. M. F. Glasser *et al.*, The minimal preprocessing pipelines for the Human Connectome Project. *Neuroimage* **80**, 105–124 (2013).
57. T. E. J. Behrens, H. J. Berg, S. Jbabdi, M. F. S. Rushworth, M. W. Woolrich, Probabilistic diffusion tractography with multiple fibre orientations: What can we gain? *Neuroimage* **34**, 144–155 (2007).
58. S. Ren *et al.*, Nonparametric bootstrapping for hierarchical data. *J. Appl. Stat.* **37**, 1487–1498 (2010).
59. V. Saravanan, G. J. Berman, S. J. Sober, Application of the hierarchical bootstrap to multi-level data in neuroscience. *Neuron Behav. Data Anal. Theory.*, 3 (2020).
60. B. Efron, R. Tibshirani, Bootstrap methods for standard errors, confidence intervals, and other measures of statistical accuracy. *Stat. Sci.* **1**, 54–75 (1986).
61. K. F. K. Wong *et al.*, Robust time-varying multivariate coherence estimation: Application to electroencephalogram recordings during general anesthesia. *Annu. Int. Conf. IEEE Eng. Med. Biol. Soc.*, 4725–4728 (2011).
62. S. N. Lahiri, *Resampling Methods for Dependent Data* (Springer Science & Business Media, 2013).
63. I. T. Jolliffe, *Principal Component Analysis* (Springer Science & Business Media, 2013).
64. C. A. Field, A. H. Welsh, Bootstrapping clustered data. *J. R. Stat. Soc. Series B Stat. Methodol.* **69**, 369–390 (2007).
65. J. E. Iglesias *et al.*, A probabilistic atlas of the human thalamic nuclei combining ex vivo MRI and histology. *Neuroimage* **183**, 314–326 (2018).
66. S. De Simoni *et al.*, Altered caudate connectivity is associated with executive dysfunction after traumatic brain injury. *Brain* **141**, 148–164 (2018).
67. T. Mitsuhashi *et al.*, Dynamic tractography-based localization of spike sources and animation of spike propagations. *Epilepsia* **62**, 2372–2384 (2021).
68. E. G. Jones, *The Thalamus* (Springer Science & Business Media, 2012).
69. V. S.Weiner *et al.*, 10-Hz cross-spectral matrices from intracranial electrode recordings before and after loss of consciousness during propofol-induced general anesthesia [Data set]. *Zenodo*. https://doi.org/10.5281/zenodo.7657814. Deposited 20 February 2023.